Synthesis and Second-Harmonic Generation Studies of Noncentrosymmetric Gold Nanostructures

Marie L. Sandrock, Charles D. Pibel,† Franz M. Geiger,‡ and Colby A. Foss, Jr.*

Department of Chemistry, Georgetown University, Washington, District of Columbia 20057

Received: December 2, 1998; In Final Form: February 12, 1999

Noncentrosymmetric gold nanoparticle structures were prepared in porous anodic aluminum oxide films via a modified template synthesis procedure. The noncentrosymmetric structures are defined by two gold particles in close proximity (ca. 22 ± 8 nm end to end) within a single host oxide pore, one having average dimensions of $a = 37 \pm 6$ nm and $b = 26 \pm 3$, and the other having dimensions of $a = 27 \pm 5$ nm and $b = 26 \pm 3$ nm, where a is the axial length and b is the diameter of the quasi-cylindrical structures. Linear UV/vis polarization spectra of the gold particle/porous alumina film composites show plasmon resonance bands whose λ_{max} incidence angle dependence is similar to composites containing centrosymmetric gold structures, where the incidence angle is defined with respect to the surface normal. Second harmonic generation (SHG) studies using an incident wavelength of 780 nm indicate that SHG intensities under s-polarization are low and independent of incidence angle (θ) for composites containing centrosymmetric and noncentrosymmetric gold nanostructures. However, in p-polarization, both composites show an increase in SHG counts with θ, with the noncentrosymmetric structures showing a higher SHG signal than their centrosymmetric counterparts. These results are consistent with local-field enhancements arising from long particle axis dipolar plasmon resonances.

Introduction

Metal particles of nanoscopic dimensions have played an interesting role in materials technology ever since the first gold-laden "ruby glass" was manufactured over three centuries ago.[1] Many metals in nanoscopic form strongly absorb and scatter visible light, and therefore give rise to a rich variety of colors. They have thus been used as pigments in the fine arts,[1−3] photographic development, and in industrial metal colorizing processes.[5,6] Over the past two decades, interest in nanoscopic metal particles has grown well beyond aesthetic considerations, as they find application in selective solar materials,[7−9] cytology[10] and molecular biology,[11] surface-enhanced spectroscopy,[12−20] and nonlinear optics.

It is well-known that the wavelength of maximum optical extinction, as well as the wavelength of optimal local electric field enhancement, depends on such factors as the size, shape, and orientation of the particle, as well as spacing between particles.[16−18] Thus, the improved application of nanoscopic metal structures in the aforementioned areas, as well as the prospect of their application in new areas of research and technology, depends on our ability to control these features.

There are many methods for preparing nanoscopic particles of nominally spherical geometry.[23−28] Methods for preparing uniformly nonspherical metal particles are less numerous, but include the grazing incidence vacuum deposition methods of Liao,[29] and the template synthesis methods developed by Moskovitz[30,31] and Martin.[32,33] We recently discussed extensions of the template synthesis method, whereby noncentrosymmetric metal pairs[34] and metal−semiconductor[35] structures are prepared in the pores of anodic aluminum oxide films.

Our interest in composites containing noncentrosymmetric nanostructures arises in part because they represent nanoscale analogues to molecular structure-based second-order nonlinear optical materials. It is well-known that within the dipole approximation,[36] materials possessing inversion symmetry will not exhibit second-order nonlinear optical effects. Indeed, many studies of the nonlinear optical properties of nanometal composite systems have focused on third-order effects.[21−23] Studies of second-order processes have been limited to metal nanostructures at interfaces, which necessarily remove inversion symmetry.[37−43] An interesting exception is the study by Leitner, who employed a two-stage vacuum deposition procedure to prepare silver particles of low symmetry on glass substrates.[44] However, the significant second harmonic generation (SHG) intensities observed under normal incidence excitation could not be specifically attributed to particle asymmetry, and may have been the result of local field enhanced magnetic dipole and quadrupole modes.[44]

In this paper, we describe the details of the synthesis of noncentrosymmetric gold particle pair structures. We also discuss the UV/vis/near-IR linear polarization spectra of noncentrosymmetric gold particle/porous aluminum oxide film composites, and their symmetric gold particle analogues. Finally, we present the first results of a study of SHG from these composite materials.

Experimental Section

Porous Anodic Alumina Film Preparation. Aluminum plates (Aldrich 99.999%, 10 cm × 10 cm × 1 mm) were first electropolished in a cell containing 2 L of 2:3 (v/v) mixture of sulfuric acid (96% Mallinckrodt) and phosphoric acid (85% Mallinckrodt). The cathode consisted of a lead plate (6 cm × 15 cm × 2 mm). The aluminum anode was masked with

* Corresponding author.
† Current address: Department of Chemistry, American University, Washington, DC 20016.
‡ Current address: Department of Chemistry, Massachusetts Institute of Technology, Cambridge, MA 02139.

10.1021/jp9845874 CCC: $18.00
Published on Web 03/18/1999

adhesive tape (3M mailing tape no. 23-8043) such that only ca. 100 cm^2 of aluminum remained exposed. The temperature of the electropolishing solution was 75 °C, and 10 A was delivered to the cell for ca. 3 min using a Sorenson DCR300-9B power supply. The polished aluminum plate was then immersed in deionized water to rinse.

The electrochemical preparation of the nanoporous alumina films utilized a two-electrode temperature-controlled anodization cell. Within the cell, stainless steel coils connected to an external circulation refrigerator bath (1:1 ethylene glycol/water mixture) maintained a constant temperature of the acid bath at 0 °C. Lead foil (6.5 cm × 14 cm × 2 mm) served as the cathode and the polished plate (100 cm^2 of exposed aluminum) was the anode. The supporting electrolyte was 6% sulfuric acid (prepared from 96% Mallinckrodt). The anodization cell was constantly stirred and a programmable power supply (Kepco ABC 25-4DM) provided a potential of 20 V. The anodic aluminum oxide film was grown (through the oxidation of aluminum) for a period of 14 h to produce pores with a 32 nm diameter and a film thickness of 40−60 μm.

Separation of the alumina film from the anode was achieved using a voltage reduction procedure which creates small branched pores[45] in the barrier layer of the oxide film, which makes this layer vulnerable to acid dissolution. The reduction occurred in gradual 5% decrements from 20 to 2 V and lasted approximately 1.5 h. After each reduction step, the current was allowed to rise to at least 85% of its previous value. After the reduction, the alumina films were placed in a 25% (V/V) sulfuric acid bath (96% Mallinckrodt) for oxide detachment, which lasted ca. 3 h. The films were then rinsed with deionized water, ethanol, and acetone, and air-dried. The thickness of the alumina nanoporous film was determined by a micrometer (Mitutoyo).

Nanoparticle Preparation. The porous alumina membranes were used as a template to synthesize gold particles of different symmetries.[46] The barrier side of the film was sputtered with ca. 45 nm of silver using an Anatech Hummer 10.2 plasma deposition device. The silver-coated oxide film was then attached to a three-electrode cell equipped with an Ag/AgCl reference electrode and a platinum mesh counter electrode. The power source was an EG&G Princeton Applied Research Model 273A potentiostat. Nitrogen was purged into the system for mixing.

A 0.80−1.27 C/cm^2 foundation of silver was potentiostatically deposited over a 3.14 cm^2 area of porous oxide from a silver thiocyanate plating solution[47] at −0.6 V vs Ag/AgCl. This foundation ensured that the subsequent gold deposition would fill the 32 nm porous region of the film. After rinsing with deionized water, gold nanoparticles were formed potentiostatically at −0.9 V vs Ag/AgCl reference from Au(I) (Technic Inc., Orotemp 24 gold plating solution). 0.3 C of Au was deposited over the 3.14 cm^2 area for centrosymmetric particles. Additionally, for noncentrosymmetric particles, 0.1 C of Au was first deposited over the area, followed by another layer of Ag (0.1 C) and finally another layer of Au (0.2 C).

All of the composites were immersed in nitric acid (69−71% EM), to dissolve any silver, leaving only gold in the pores. The composite films were rinsed with deionized water, ethanol, and acetone and air-dried. The procedure for preparing both types of particle composites is summarized in Figure 1.

Nanoparticle Characterization. Transmission electron microscopy was used to characterize the dimensions of the template synthesized gold nanoparticles. Additional sample preparation was required in order to obtain TEM (transmission electron microscope) images. The gold particle composite films were embedded in a resin and heated at 70 °C for 12 h. A 70 μm section was cut using a diamond knife (SPI Inc.) and placed on a Formvar-coated Cu grid (200 mesh, EM Sciences). The samples were then examined with a JEOL 1200 EX transmission electron microscope.

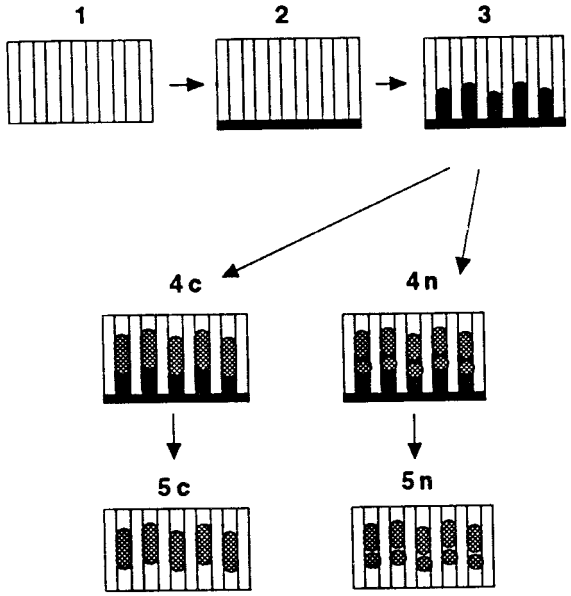

Figure 1. Schematic of nanoparticle synthesis: (1) porous anodic alumina film after detachment from Al substrate; (2) one face of alumina film coated with silver using plasma deposition; (3) electrodeposit silver foundation into pores; (4c) electrodeposit gold onto silver foundation to form centrosymmetric gold particles; (4n) electrodeposit layers of gold, silver, and then a second gold layer to form noncentrosymmetric gold particles; (5c and 5n) immerse film in nitric acid to remove silver foundation and silver spacing segments.

Linear Optical Analysis. Linear polarization spectra were collected with a Hitachi U3501 UV/vis/near-IR spectrometer equipped with a 210-2130 polarizer accessory. Sample extinction (measured as sample absorbance) was measured at 1 nm increments between 350 and 800 nm, at a bandwidth of 2 nm. In this spectral range, the U3501 employed a tungsten lamp source and photomultiplier tube detector. Spectra were obtained with the incident propagation vector normal to the composite film surfaces (incidence angle $\theta = 0$), and at incidence angles of 20°, 30°, and 45° under p-polarization. These four incidence angles correspond to an incident electric field which is perpendicular, 70°, 60°, and 45°, respectively, to the particles' rotation axis. The configuration of the linear optical experiment is shown schematically in Figure 2.

Second Harmonic Generation Studies. The SHG studies employed a high repetition rate femtosecond titanium−sapphire laser system, which was constructed following the design of Murnane[48] and pumped by an argon ion laser (Spectra Physics 2060). The Ti:sapphire laser has a tunable output range of 710−900 nm. We restricted our initial studies to an output of 780 nm. The pulse widths employed were ca. 150 fs at an 80 MHz repetition rate. The average power was 100−300 mW, corresponding to an energy of ca. 3 nJ per pulse.

Figure 3 shows a schematic of the optical bench used in the SHG studies. The 780 nm source line was split and directed to a sample and reference line. A slide-mounted mirror allowed for the alternate detection of sample and reference signals using a single monochromator and detection system. The reference material consisted of a slurry of potassium dihydrogen phosphate (KDP, Fisher Scientific) in decahydronaphthalene (Aldrich 99%).

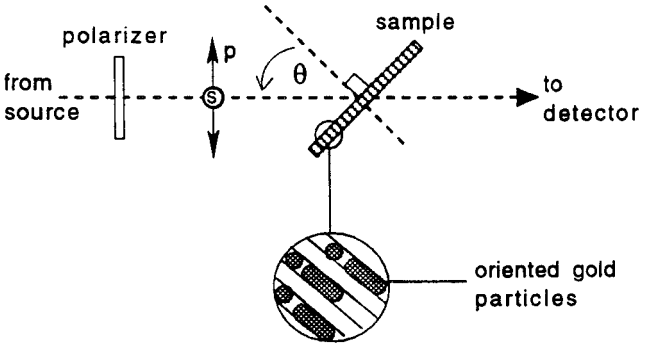

Figure 2. Schematic of polarization spectroscopy setup. The sample film is rotated about an axis perpendicular to the page. The angle of incidence is indicated by θ. p-Polarization corresponds to an incident electric field polarized in the plane on the page. s-Polarization corresponds to an electric field oscillating perpendicular to the page.

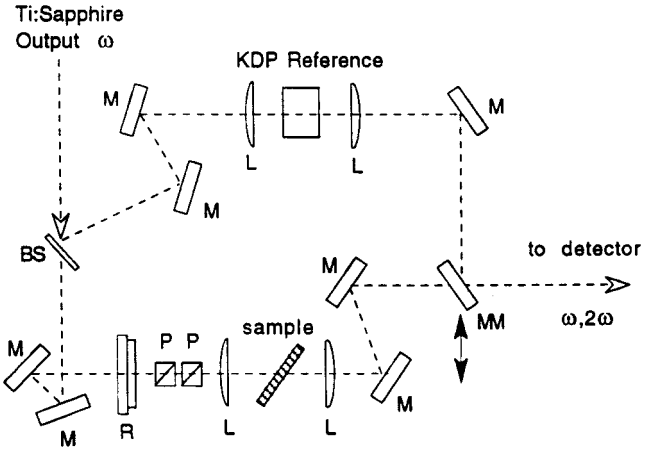

Figure 3. Schematic of second harmonic generation optics bench. Meaning of symbols: BS, beam splitter; M, stationary mirror; R, retarder; P, polarizer; L, lens; MM, moving mirror to select sample or reference beam for measurement.

For the gold particle/porous alumina sample line, the source polarization was controlled by a variable retarder (Meadowlark Optics) and a Glan laser polarizer (Zeta International). A second polarizer was incorporated to attenuate the beam to an average power of 24 mW, which results in a fluence well below each sample's measured optical damage threshold (ca. 40 mW). The SHG signal was measured for polarizations at 0° (p) and 90° (s) with respect to the plane of incidence. The incidence angle, θ, was varied by rotating the composite film along an axis perpendicular to the tabletop. Three trials were performed for both composite materials, each focusing on a different portion of the film. This step is necessary, as the composite films are not isotropic materials.

The SHG signal (from sample and reference lines) was focused into a monochromator (Oriel 77298) which contained a grating (1200 lines/mm) blazed at 350 nm, and a filter placed before monochromator (transmitted range 353−462 nm). The monochromator output was set at 390 nm (band-pass = 10.0 nm) and the SHG photons were detected using a Hamamatsu R5858 PMT with a discriminator (F-100T Advanced Research Instruments). The pulses due to single SHG photons were counted using an I/O board (Computer Boards Inc. Model CIO-DIO24) over a 1 s collection interval.

Results and Discussion

Figure 4 shows TEM images of cross-sections of porous anodic alumina films containing centrosymmetric and noncentrosymmetric gold structures. The noncentrosymmetric structures consist of two segments of gold, one roughly spherical and the other rodlike in geometry. The longer segments show an average length $a = 37 \pm 6$ nm, and the smaller segments have an average length $a = 27 \pm 5$ nm. The diameter of the particles is ca. 26 ± 3 nm. The separation distance between the two segments is 22 ± 8 nm. The centrosymmetric particles have an axial length $a = 54 \pm 7$ nm and diameter $b = 30 \pm 4$ nm.[49]

In Figure 5 we show the polarization spectra for the two types of gold particle composites. The numbers on the curves pertain to the angle of incidence under p-polarization. The spectra for centro- and noncentrosymmetric particle composites are generally similar in the following respects: At normal incidence ($\theta = 0$), the spectra are characterized by a plasmon resonance band centered at ca. 530−540 nm. As the angle of incidence increases, and a correspondingly greater component of the incident electric field is coincident with the long axes of the particles, a broad plasmon resonance band grows in at longer wavelengths. For the centrosymmetric structures, the long axis resonance is centered at ca. 640 nm. For the noncentrosymmetric pair particles, the long axis resonance is centered at ca. 650 nm.

The observed dichroic properties of the composite films at nonnormal incidence under p-polarization are consistent with the results of earlier studies on nanoscopic gold rods oriented in polyethylene films,[50] and can be understood in terms of the quasi-static limit expression for particle polarizability (α):

$$\alpha = \frac{4\pi ab^2}{L_x}\left(\frac{\tilde{\epsilon}_m - \tilde{\epsilon}_o}{\tilde{\epsilon}_m + \kappa\tilde{\epsilon}_o}\right) \quad (1)$$

where a and b are the semimajor and semiminor axes, respectively, of an ellipsoid of revolution. The complex dielectric functions of the metal and host medium are $\tilde{\epsilon}_m$ and $\tilde{\epsilon}_o$, respectively. The screening factor κ is related to the depolarization factor L_x via $\kappa = L_x^{-1} - 1$, which in turn can be calculated from a and b.[51] For free-electron metals, the real part of the complex dielectric constant is generally negative, and monotonically decreasing with wavelength in the visible spectrum. Thus, as the screening factor κ increases, the plasmon resonance maximum is expected to shift to longer wavelengths.[51]

For the spectra shown in Figure 5, the emergence of a long-wavelength resonance with increasing incidence angle under p-polarization is consistent with a long-axis screening factor ($\kappa_{||}$) greater than 2 (the value for spherical particles). The 0.096 C cm^{-2} of Au(I) deposited in the centrosymmetric particle synthesis results in rodlike particles of aspect ratio $a/b \approx 1.8$; this corresponds to a screening factor $\kappa_{||} = 3.6$. On the other hand, in the noncentrosymmetric particle synthesis, the distribution of 0.096 C cm^{-2} into two segments results in one particle being roughly spherical ($a/b \approx 1$, $\kappa = 2$), and one being moderately rodlike ($a/b \approx 1.4$, $\kappa_{||} = 2.8$). The rodlike segment alone should give rise to spectral dichroism, but with a long axis λ_{max} at a shorter wavelength than exhibited by the centrosymmetric particles. An isolated spherelike segment should show no dichroism. Apparently, the similarity of the long axis λ_{max} values for the centrosymmetric and noncentrosymmetric particle pair composites arises from the close proximity of the rod- and spherelike segments in the latter system. We will discuss particle spacing effects on linear polarization spectra in a later publication.[52]

In the SHG studies, we examined the same centro- and noncentrosymmetric Au particle alumina composite samples considered in the polarization spectroscopic measurements. For both sample types, we measured SHG intensities at normal

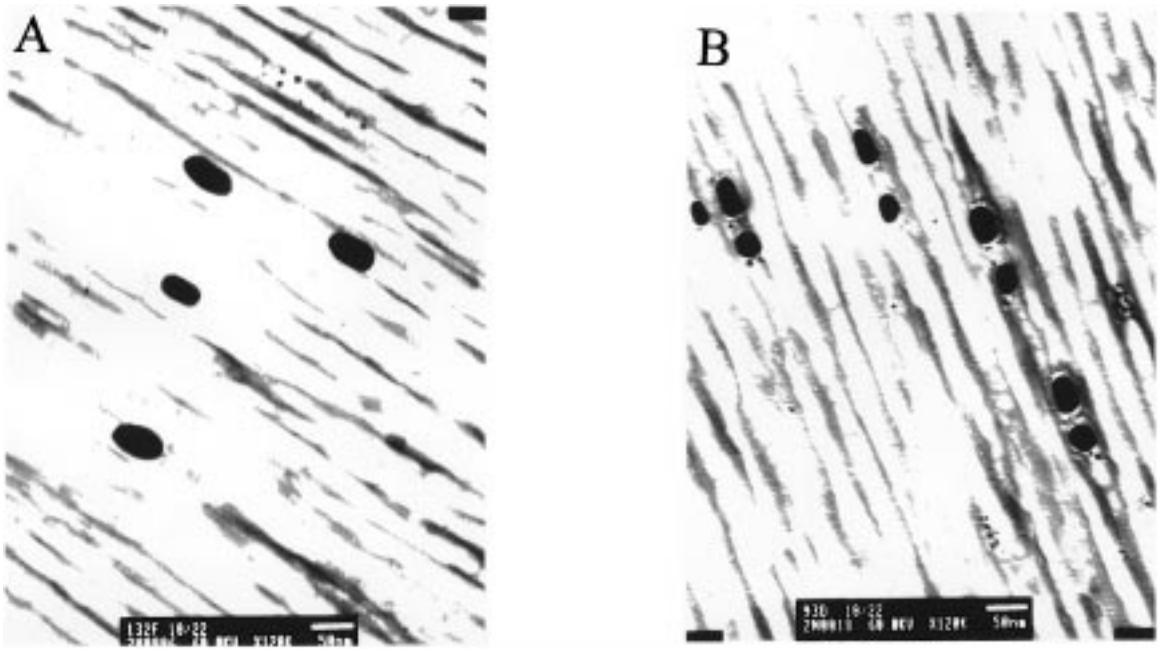

Figure 4. Transmission electron microscope images: (A) 0.1 C cm^{-2} Au centrosymmetric Au particles in alumina host; (B) 0.10 C cm^{-2} noncentrosymmetric Au particles in alumina host (0.06 C cm^{-2} Au(I) deposited for larger segment, 0.03 C cm^{-2} Au(I) deposited for smaller segment). Scale bar in both cases corresponds to 50 nm.

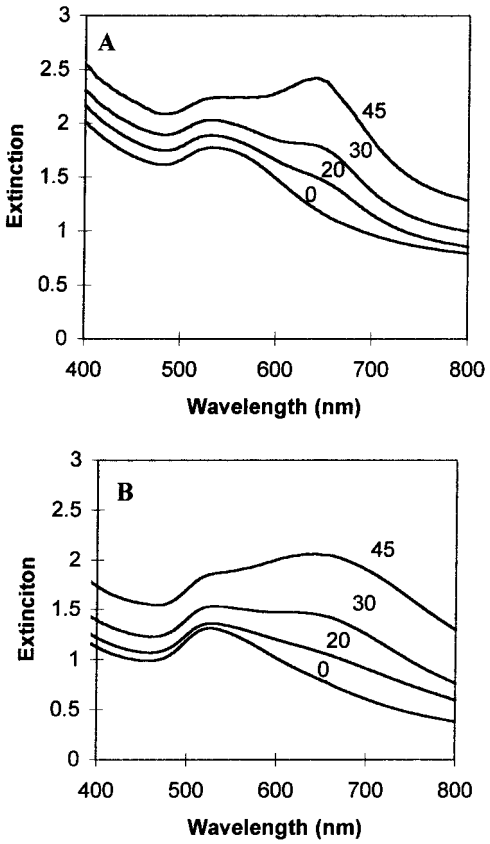

Figure 5. UV/visible p-polarization spectra: (A) centrosymmetric Au particle/alumina composite; (B) noncentrosymmetric Au pair/alumina composite. Incidence angles indicated next to curves. "Extinction" abscissa is unitless and corresponds to spectrometer "absorbance" output. However, the measured extinction includes losses due to absorption, scattering and reflectance. All measurements were made in double-beam mode, with no material in the reference beam.

incidence and at incidence angles of 20°, 30°, and 40° under s- and p-polarization. Figure 6 summarizes the results of these studies. In all cases, the SHG counts from the Au particle/

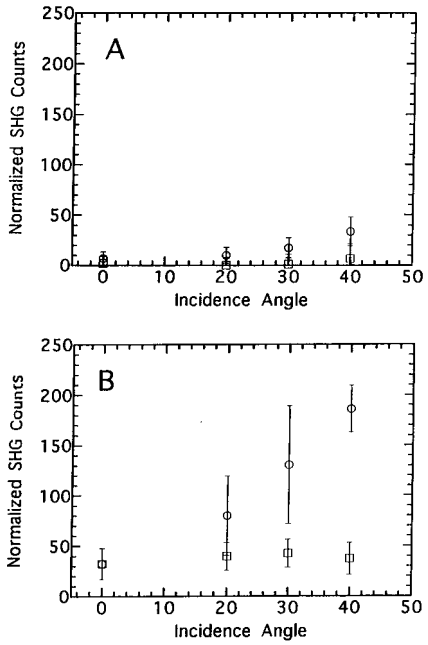

Figure 6. Second harmonic generation (SHG) intensity as a function of the angle of incidence. Open circles correspond to p-polarized incident light. Boxes correspond to s-polarized excitation. (A) Centrosymmetric Au particle/alumina composite. (B) Noncentrosymmetric pair particle/alumina composite.

alumina samples are normalized against the counts from the KDP reference. The error bars are based on the results of measurements on three different locations of the composite films. We should also note that SHG studies on porous oxide films containing no gold were also performed, and showed negligible signals for all incidence angles and polarizations.

With our laser system, SHG yields range from 4 to 210 counts. For the centrosymmetric particle composite (Figure 6A), the SHG counts are small for both s-polarization (ca. 8 counts), and p-polarization (ca. 8−30 counts). The SHG signal for p-polarized excitation shows a small increase with incidence angle θ. In s-polarization, the SHG signal is constant within

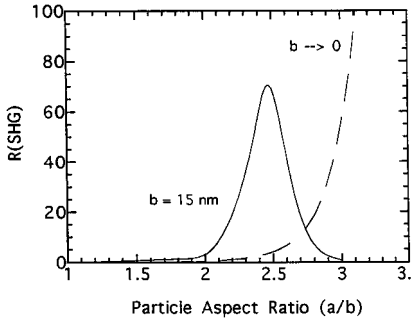

Figure 7. Calculated SHG local field enhancement factors (based on eq 2) as a function of particle aspect ratio for gold particles where incident wavelength is 780 nm, and second harmonic output wavelength is 390 nm. Dashed curve corresponds to quasistatic limit where particle dimensions are assumed to be negligibly small relative to λ. Solid curve: SHG local field enhancement calculation taking into account dynamic depolarization and radiation damping in rodlike particles of radius 15 nm.

experimental error. In the noncentrosymmetric particle composite (Figure 6B), the SHG counts under s-polarization are, within experimental error, constant with θ (ca. 30 counts). However, in p-polarization, the SHG counts increase dramatically with incidence angle (ca. 30−200 counts). At $\theta = 40°$, the normalized SHG counts are about 6 times higher than the corresponding signal for the centrosymmetric particle composite.

The observed dependence of the SHG signal on incidence angle for the noncentrosymmetric particles under p-polarization is reasonable in two respects. First, as the incidence angle increases, the component of the incident electric field directed along the asymmetry axis (the axis perpendicular to the rotation axis of the rod) of the gold pair-particle structure increases. Second, enhancement effects associated with the long-axis dipolar plasmon resonance are increased with θ. For the s-polarization case, the electric field is always perpendicular to the asymmetry axis, and consequently, there is no dependence of SHG on θ.

The connection between the linear spectra and the local field enhancement factor R for SHG can be seen in the approximate expression[37,39]

$$R = |L^2(\omega)L(2\omega)| \tag{2a}$$

where the function L is given by

$$L(\omega) = \left(\frac{\epsilon_o(\omega)}{L_x(\epsilon_m(\omega) + \kappa\epsilon_o(\omega))}\right)^2 \tag{2b}$$

Thus, the local field and R are large when either the fundamental frequency (ω) or the second harmonic (2ω) is close to a plasmon resonance.

We calculated the local field enhancement factors for gold rods of various aspect ratios in a nonabsorbing host (refractive index $n_o = 1.33$ at both $\lambda = 780$ nm and $\lambda = 390$ nm). The optical constants of gold were taken from Johnson and Christy.[53] The enhancement factor curves shown in Figure 7 pertain specifically to the case where the incident electric field is parallel to the long (rotation) axis of the gold particle. In our SHG studies, normal incidence ($\theta = 0$) corresponds to the case where the electric field component along the long axis is zero; however, as the incidence angle increases under p-polarization, the electric field component along the long axis also increases. The influence of long-axis local field enhancements increases accordingly.

Figure 7 shows local field enhancements based on two theoretical treatments. The dashed curve shows the quasi-static limit treatment based on eq 2, where the gold particle dimensions are assumed to be negligibly small relative to λ. According to this treatment, local field enhancement R becomes significant only for particles with aspect ratios greater than ca. 2.5. However, if particle size is incorporated into L_x and κ,[17,54] R becomes significant at smaller aspect ratios (see solid curve in Figure 7).

The local field model also explains in part the observed SHG in the centrosymmetric particle composites. From the dipole approximation treatment of nonlinear optical processes, we would not expect to observe SHG from small centrosymmetric particles.[36,55] However, metal spheres a few nanometers in diameter or larger can support quadrupolar electric and magnetic induction modes, which in theory can give rise to SHG.[56−58] Since the dimensions of the Au particles in this study are such that quadrupole modes would necessarily be quite weak (we do not observe quadrupole bands in the linear spectra), local field enhancements must play an important role in the SHG from the centrosymmetric particles. The observation that SHG counts increase for p-polarized excitation (Figure 6A) is consistent with a local field enhanced process.

Finally, it is significant to note that in the comparison of centro- and noncentrosymmetric particle composites, the latter system shows higher SHG counts in s-polarization even at normal incidence ($\theta = 0$). In an ideal composite structure where the cylindrical pores (and therefore the template-synthesized particles) are uniformly aligned perpendicular to the film surface, we would expect the SHG counts from centro- and noncentrosymmetric composites to be very similar. In fact, the pores are not perfectly aligned and the film surfaces are not perfectly flat. Thus, in s-polarization, there will be some fraction of particles which experience a nonzero component of the incident electric field along their asymmetry axis. While we have not yet quantified the distribution of the particle orientation within the composites, it should be emphasized that the net deviation from perpendicular orientation (relative to the average film surface plane) must be small, as we do not detect long-axis plasmon resonance bands in the normal incidence linear spectra (Figure 5).

Conclusions

We have prepared centro- and noncentrosymmetric Au particle structures in porous anodic alumina hosts using an electrochemical template synthesis method. The linear polarization spectra of the Au particle/anodic alumina composites reveal that both types of composites are dichroic under p-polarization for incidence angles $\theta > 0$. In the case of the noncentrosymmetric Au particle pair structures, the strong linear dichroism arises in part because of the close proximity of the spherical and rodlike segments in the porous host.

Second harmonic generation studies of the centro- and noncentrosymmetric particle composites reveal that the latter system gives rise to stronger SHG signals, and that the SHG intensity under p-polarized excitation increases with incidence angle (i.e., as the component of the incident electric field parallel to the asymmetry axis increases). These observations are consistent with local field enhancements arising from long-axis dipolar plasmon resonances. The weak SHG observed in the centrosymmetric particle system may arise from quadrupole induction modes.

Quasistatic theory calculations of the local field enhancement factors for SHG from gold particles suggest that enhancements become appreciable for particle aspect ratios greater than ca. 3, which is larger than the value associated with the particles

considered in this study. However, calculations that take into account absolute particle size (and therefore such effects as dynamic depolarization and radiation damping[17,54]) show that local field enhancements may be optimal at smaller aspect ratios. Studies of particle shape and size effects on SHG are in progress.

Acknowledgment. The authors are grateful to the National Science Foundation for its support of this work (Grant DMR 9625151). M.L.S. also acknowledges the support of the ARCS Foundation. F.M.G. thanks the National Aeronautics and Space Administration for a Global Change Graduate Student Fellowship in Earth Science Systems. Electron microscopy support was provided by the Lombardi Cancer Center Microscopy and Imaging Shared Resource (U.S. Public Health Services Grant 2P30-CA-51008).

References and Notes

(1) (a) Mehlman, F. *Phaidon Guide to Glass*; Prentice Hall: Englewood Cliffs, NJ, 1983. (b) Moore, N. H. *Old Glass: European and American*; Tudor Publishers: New York, 1935.

(2) Lam, D. M.-K.; Rossiter, B. W. *Sci. Am.* **1991**, Nov, 80−85.

(3) Lam, D. M.-K.; Baran, A. *Sci. Am.* 1991, Nov, 136−147.

(4) Carroll, B. H.; James, T. H. *Introduction to Photographic Theory: the Silver Halide Process*; Wiley: New York, 1980.

(5) Goad, D. W.; Moskovits, M. *J. Appl. Phys.* **1978**, *49*, 2929.

(6) Sato, T.; Sakai, S. *Trans. 1nst. Metal Finishing* **1979**, *57*, 43.

(7) Andersson, A.; Hunderi, O.; Granqvist, C. G. *J. Appl. Phys.* **1980**, *51*, 754.

(8) Niklasson, G. A. *Solar Energy Mater.* **1988**, *17*, 217.

(9) Sathiaraj, T. S.; Thangaraj, R.; Al-Sharbaty, H.; Agnihotri, O. P. *Thin Solid Films* **1991**, *195*, 33.

(10) Beesley, J. E. *Proc. R. Microsc. Soc.* **1985**, *20*, 187.

(11) (a) Storhoff, J. J.; Mirkin, C. A.; Letsinger, R. L. *J. Am. Chem. Soc.* **1998**, *120*, 1959. (b) Mucic, R. C.; Storhoff, J. J.; Mirkin, C. A. *Nature* **1996**, *382*, 607.

(12) Fleischmann, M.; Hendra, P. J.; McQuillan, A. J. *Chem. Phys. Lett.* **1974**, *26*, 163.

(13) McQuillan, A. J.; Hendra, P. J.; Fleischmann, M. *J. Electroanal. Chem.* **1975**, 65, *933*.

(14) Chang, R. K., Furtak, T. E., Eds. *Surface Enhanced Raman Scattering*; Plenum Press: New York, 1982.

(15) Moskovits, M. *Rev. Mod. Phys.* **1985**, *57*, 783.

(16) Kerker, M., Ed. *Selected Papers on Surface-Enhanced Raman Scattering*; SPIE Optical Engineering Press: Bellingham, WA, 1990.

(17) Zeman, E.; Schatz, G. C. *J. Phys. Chem.* **1987**, *91*, 634.

(18) Bergman, D. J.; Nitzan, A. *Chem. Phys. Lett.* **1982**, *88*, 409.

(19) Freeman, R. G.; Grabar, K. C.; Allison, K. J.; Bright, R. M.; Davis, J. A.; Githrie, A. P.; Hommer, M. B.; Jackson, M. A.; Smith, P. C.; Walter, D. G.; Natan, M. J. *Science* **1995**, 267, *1629*.

(20) Chumanov, G.; Sokolov, K.; Gregory, B. W.; Cotton, T. M. *J. Phys. Chem.* **1995**, *99*, 9466.

(21) Hache, F.; Ricard, D.; Flytzanis, C. *J. Opt. Soc. Am. B* **1986**, *3*, 1647.

(22) Hache, F.; Ricard, D.; Flytzanis, C.; Kreibig, U. *Appl. Phys. A* **1988**, *47*, 347.

(23) Flytzanis, C.; Hache, F.; Klein, M. C.; Ricard, D.; Roussingnol, Ph. In *Progress in Optics*; Wolf, E., Ed.; North-Holland: Amsterdam, 1991; Vol. 29, pp 323−411.

(24) Kosuka, H.; Sakka, S. *Chem Mater.* **1993**, *5*, 222.

(25) Handley, D. A. In *Colloidal Gold: Principles, Methods and Applications*; Hayat, M. A., Ed.; Academic Press: San Diego, CA, 1989; Vol. 1, pp 13−32.

(26) Mulvaney, P.; Linnert, T.; Henglein, A. *J. Phys. Chem.* **1991**, *95*, 7843.

(27) Brust, M.: Walker, M.; Bethell, D.; Schiffrin, D.; Whyman, R. *J. Chem. Soc., Chem. Commun.* **1994**, 801.

(28) Leff, D. V.; Ohara, D. C.; Heath, J. R.; Ferrell, T. C. *J. Opt. Soc. Am. B* **1988**, *4*, 927.

(29) Liao, P. F. In *Surface Enhanced Raman Scattering*; Chang, R. K., Furtak, T. E., Eds.; Plenum Press: New York, 1982. See also: Buncick, M. C.; Warmack, R. J.; Ferrell, T. C. *J. Opt. Soc. Am. B* **1988**, *4*, 927.

(30) Preston, C. K.; Moskovits, M. *J. Phys. Chem.* **1988**, *92*, 2957.

(31) Preston, C. K.; Moskovits, M. *J. Phys. Chem.*, **1993**, *97*, 8405.

(32) Tierney, M. J.; Martin, C. R. *J. Phys. Chem.* **1989**, *93*, 2878.

(33) Foss, C. A., Jr.; Hornyak, G. L.; Stockert, J. A.; Martin, C. R. *J. Phys. Chem.* **1994**, *98*, 2963.

(34) Sandrock, M. L.; Foss, C. A., Jr. The 193rd Meeting of the Electrochemical Society, Abstract No. 285, May 1998, San Diego.

(35) El-Kouedi, M.; Foss, C. A., Jr. The 193rd Meeting of the Electrochemical Society, Abstract No. 9, May 1998, San Diego.

(36) Boyd, R. W. *Nonlinear Optics*; Academic Press: Boston, 1992.

(37) Guyot-Sionnest, P.; Shen, Y. R. *Phys. Rev. B* **1988**, *38*, 7985.

(38) Chen, C. K.; deCastro, A. R. B.; Shen, Y. R. *Phys. Rev. Lett.* **1981**, *46*, 145.

(39) Berkovic, G.; Efrima, S. *Langmuir* **1993**, *9*, 355.

(40) Steinmüller-Nethl, D.; Höpfel, R. A.; Leitner, A.; Aussenegg, F. R.; Wokaun, A. *Appl. Phys. A* **1993**, *57*, 261.

(41) Götz, T.; Buck, M.; Dressler, C.; Eisert, F.; Träger, F. *Appl. Phys. A.* **1995**, *60*, 607.

(42) Aussenegg, F. R.; Leitner, A.; Gold, H. *Appl. Phys. A* **1995**, *60*, 97.

(43) Aktsipetrov, O. A.; Elyutin, P. V.; Fedyanin, A. A.; Nikulin, A. A.; Rubtsov, A. N. *Surf. Sci.* **1995**, *325*, 343.

(44) Leitner, A. *Mol. Phys.* **1990**, *70*, 197.

(45) Furneaux, R. C.; Rigby, W. R.; Davidson, A. P. *Nature* **1989**, *337*, 147.

(46) Foss, C. A., Jr.; Tierney, M. J.; Martin, C. R. *J. Phys. Chem.* **1992**, *96*, 9001.

(47) Shumilova, N. A.; Zutaeva, E. V. In *Encyclopedia of Electrochemistry of the Elements*; Bard, A. J., Ed.; Marcel-Dekker: New York, 1978; Vol. 8.

(48) Murnane, M.; Kapteyn, H. C.; Huang, C. P.; Asaki, M. T.; Garvey, D. *Mode-locked Ti−Sapphire Laser*; Washington State University, 1992.

(49) The dimensions of the particles were determined from TEM images. The average length, diameter, and standard deviations were determined from measurements of fifteen to twenty individual structures.

(50) Al-Rawashdeh, N. R.; Sandrock, M. L.; Seugling, C. J.; Foss, C. A., Jr. *J. Phys. Chem. B* **1998**, *102*, 361.

(51) The plasmon resonance maximum occurs at the wavelength where the real part of the metal dielectric constant ϵ'_m equals the quantity, $-\kappa\epsilon'_o$, where ϵ'_o is the real part of the host dielectric constant. κ is related to the particle depolarization factor L_x via the relation $\kappa = L_x^{-1} - 1$. If the gold particles are treated as ellipsoids of revolution (semimajor axis a and radius b), L_x for an electric field incident along a given axis x ($= a$ or b) can be estimated via the relation $L_x = x/(1/a + 2/b)$. See for example: van de Hulst, H. C. *Light Scattering by Small Particles*; Dover: New York, 1980.

(52) Sandrock, M. L.; Foss, C. A., Jr. Manuscript in preparation.

(53) Johnson, P. B.; Christy, R. W. *Phys. Rev. B* **1972**, *6*, 4370.

(54) Meier, M.; Wokaun, A. *Opt. Lett.* **1983**, *8*, 851.

(55) Within the dipole approximation, SHG from centrosymmetric particles is also possible provided that the particle dimensions are comparable to the coherehnce length of the SHG process (see for example: Yan, E. C. Y.; Liu, Y.; Eisenthal, K. B. *J. Phys. Chem. B* **1998**, *102*, 6331). For the conditions employed in our experiments, the coherence length is much smaller than the gold particle dimensions.

(56) Dewitz, J. P.; Hubner, W.; Bennemann, K. H. *Z. Phys. D* **1996**, *37*, 75.

(57) Östling, D.; Stampfli, P.; Benneman, K. H. *Z. Phys. D* **1993**, *28*, 169

(58) Hua, X. M.; Gersten, J. I. *Phys. Rev. B* **1986**, *33*, 3756.